

Effects of isoelectronic Ru substitution at the Fe site on the energy gaps of optimally F-doped SmFeAsO

D. Daghero,¹ M. Tortello,¹ G.A. Ummarino,¹ V.A. Stepanov,²
F. Bernardini,³ M. Tropeano,⁴ M. Putti,^{5,4} and R.S. Gonnelli¹

¹*Dipartimento di Scienza Applicata e Tecnologia, Politecnico di Torino, 10129 Torino, Italy*

²*P.N. Lebedev Physical Institute, Russian Academy of Sciences, 119991 Moscow, Russia*

³*Dipartimento di Fisica, Università di Cagliari, 09042 Monserrato (CA), Italy*

⁴*Dipartimento di Fisica, Università di Genova, via Dodecaneso 33, 16146 Genova, Italy*

⁵*CNR-SPIN, Corso Perrone 24, 16152 Genova, Italy*

We studied the effects of isoelectronic Ru substitution at the Fe site on the energy gaps of optimally F-doped SmFeAsO by means of point-contact Andreev reflection spectroscopy. The results show that the SmFe_{1-x}Ru_xAsO_{0.85}F_{0.15} system keeps a multigap character at least up to $x = 0.50$, and that the gap amplitudes Δ_1 and Δ_2 scale almost linearly with the local critical temperature T_c^A . The gap ratios $2\Delta_i/k_B T_c$ remain approximately constant only as long as $T_c \geq 30\text{K}$, but increase dramatically when T_c decreases further. This trend seems to be common to many Fe-based superconductors, irrespective of their family. Based on first-principle calculations of the bandstructure and of the density of states projected on the different bands, we show that this trend, as well as the T_c dependence of the gaps and the reduction of T_c upon Ru doping, can be explained within an effective three-band Eliashberg model as being due to a suppression of the superfluid density at finite temperature that, in turns, modifies the temperature dependence of the characteristic spin-fluctuation energy.

PACS numbers: 74.50.+r , 74.70.Dd, 74.45.+c

INTRODUCTION

The discovery of Fe-based superconductors (FeBS) [1] with T_c as high as 55 K has shown that cuprates no longer represent the only class of high- T_c compounds. One of the reasons of the great excitement in the scientific community and of the impressive amount of work produced up to now is certainly that these materials give the opportunity to study high- T_c superconductivity in different systems, in the hope to enucleate its key elements. The parent stoichiometric compounds of most FeBS are not superconducting (with few exceptions, like LiFeAs and LaFePO) but display a metallic behaviour (as opposed to the Mott insulating state of cuprates) and feature a long-range antiferromagnetic (AFM) spin-density-wave (SDW) order. Superconductivity appears upon doping and, in some systems, also by applying pressure; however, the order of the transition between magnetic and superconducting phases seems not to be universal though increasing evidences are being collected of a region of co-existence of superconductivity and magnetism. Contrary to cuprates (where the superconducting region in the phase diagram is dome-shaped and the maximum T_c corresponds to a well-defined “optimal” doping) in FeBS superconductivity sometimes appears with T_c already very close to the maximum and shows a weak doping dependence in a broad doping range. A central feature of FeBS – which is tightly connected to the origin of superconductivity according to the most widely accepted theories – is their multiband character. They feature indeed two or three hole pockets around the Γ point of the first Brillouin

zone and two electron pockets at the M point (in the folded Brillouin zone) [2, 3]. In 1111 compounds, all the relevant Fermi surface sheets are weakly warped cylinders parallel to the k_z axis (as expected in a layered material) while a greater degree of three-dimensionality is observed in 122 compounds. These multiple bands and their almost perfect nesting in the parent compound explain the AFM instability. The weakening of the nesting induced by doping instead leads to spin fluctuations that would act as the glue for the formation of Cooper pairs. A spin-fluctuation mediated pairing would be mainly *inter-band* and would favour the opening of superconducting energy gaps of different sign on different Fermi surface sheets, the so-called $s\pm$ symmetry [4]. Though many theoretical and experimental results support this theory [5, 6] there is not, up to now, a definitive proof of such a picture. Things are further considerably complicated by the fact that the electronic bandstructure is very sensitive to some fine structural parameters, like the Fe-As-Fe bond angle and more particularly the height of the pnictogen atom (h_{As}) above the Fe layer. Possibly because of this sensitivity, in many situations the gap structure of FeBS can vary considerably within the same system, giving rise to line nodes, point nodes, deep gap minima etc. [7–10]. In 1111 compounds, h_{As} has been proposed as a switch between high- T_c nodeless superconductivity and low- T_c nodal superconductivity [11].

In the effort to discriminate the effects of different parameters on the superconducting and magnetic phases of FeBS many different chemical substitutions have been performed. The main effect of aliovalent substitutions is

to dope the parent compound with charge, either electrons [12, 13] or holes [14] thus allowing to explore the phase diagram. Isovalent substitutions [15–18], instead were tried to modify the lattice structure, create “chemical pressure”, introduce disorder (acting as magnetic or non-magnetic impurities) etc. A further degree of freedom is the site of substitution, that can reside either in the spacing layer [14] or in the active one containing Fe [15–18], which is possibly directly involved in the magnetic pairing via spin fluctuations.

Here we report on point-contact Andreev-reflection spectroscopy (PCARS) measurements performed in $\text{SmFe}_{1-x}\text{Ru}_x\text{AsO}_{0.85}\text{F}_{0.15}$ with x ranging from 0 to 0.50. The considerable decrease of T_c in this series of samples has been attributed to disorder in the Fe sub-lattice [15] and/or occurrence of a short-range static magnetic order [19]. PCARS results clearly indicate the presence of a multigap character at all the investigated levels of Ru substitution. The superconducting gaps decrease approximately linearly with the local critical temperature of the contact, T_c^A but, even when the latter is reduced by a factor 5 with respect to the optimal value, they show no sign of nodes, either intrinsic or “accidental”. For both gaps, the $2\Delta/k_B T_c$ ratio is rather constant down to $T_c^A > 30\text{K}$ but then increases consistently below this critical temperature. Comparison with other results in literature indicates that many different FeBS fit in this trend, which suggests the possibility to study some properties common to different compounds in a single samples series that allows spanning a very wide range of critical temperatures. Thanks to *ab-initio* electronic structure calculations, the trend of the gaps as a function of T_c^A has been reproduced within a minimal three-band, $s\pm$ Eliashberg model. This model also takes into account the so-called “feedback” effect, i.e. the effect of the condensate on the antiferromagnetic spin fluctuations possibly responsible for the superconductivity in these compounds. The evolution as a function of T_c of the temperature dependence of the condensate necessary to reproduce the experimental data looks rather similar to that obtained from London penetration-depth measurements performed in other FeBS, particularly in the region of coexistence of superconductivity and magnetism. This fact suggests that, in agreement with ref. [19], proximity of superconductivity and magnetism in these samples might be one of the main reasons for the decrease of T_c and for the observed behavior of the energy gaps.

EXPERIMENTAL DETAILS

The polycrystalline $\text{SmFe}_{1-x}\text{Ru}_x\text{AsO}_{0.85}\text{F}_{0.15}$ samples were synthesized as described in Ref. [15]. The starting mixture of fine powder of SmAs and 99.9% pure Fe_2O_3 , RuO_2 , FeF_2 , Fe and Ru was pressed in pellets and then put through a two-step reaction process involving a first

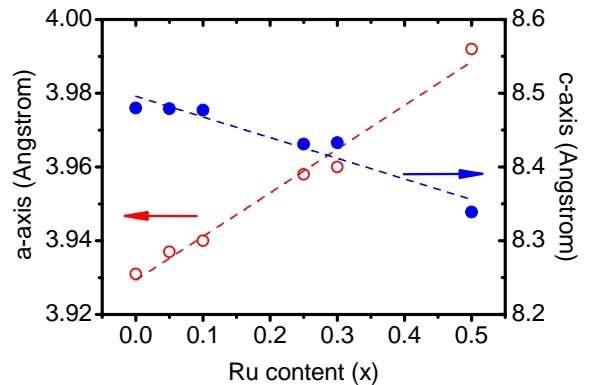


FIG. 1: Lattice constants for $\text{SmFe}_{1-x}\text{Ru}_x\text{AsO}_{0.85}\text{F}_{0.15}$ at different Ru content x . Lines are only guides to the eye.

x	T_c (K)	ρ_0 (m Ω cm)
0	52.0	0.33
0.05	42.8	0.87
0.10	21.5	1.33
0.25	28.1	1.20
0.30	13.6	1.69
0.50	13.5	0.70

TABLE I: Resistive critical temperatures and residual resistivities (defined as in ref. [15]) for $\text{SmFe}_{1-x}\text{Ru}_x\text{AsO}_{0.85}\text{F}_{0.15}$ samples at different Ru contents. T_c and ρ_0 for the samples with $x = 0.25$ and $x = 0.50$ are different from those reported in ref. [15].

heating to 450° and a second heating to $1000 - 1075^\circ$. X-ray diffraction analysis showed small amounts of SmOF (up to 6 %) in the final samples. Figure 1 shows the dependence of the lattice constants a and c on the Ru content x , indicating that Ru substitution for Fe is effective. Resistive critical temperatures and residual resistivities for the samples used in this work are reported in table I. The samples with $x = 0.25$ and $x = 0.50$ have higher T_c and much improved transport properties (namely, resistivity, magnetoresistance and Hall mobility) than those reported in ref. [15] for the same doping contents, even though they were prepared in the same way. The possible reason of this difference is under investigation. In any case, these samples were particularly suited for PCARS measurements, since the longer mean free path makes it easier to attain the spectroscopic conditions, as explained below.

Point contact spectroscopy is a local, surface-sensitive technique and it is therefore necessary to avoid any surface degradation or contamination. The samples were thus always kept in dry atmosphere, and broken to expose a clean surface prior to point-contact fabrication. The point contacts were made by putting a small drop of Ag paste on that surface, as described elsewhere [20, 21].

With respect to the standard “needle-anvil” technique, this configuration ensures a greater mechanical and thermal stability of the contacts and also allows the whole mounting for point contact to be hermetically closed in the cold head of the cryogenic insert thus avoiding any exposition to air and moisture during the transfer from the glove box (where the point contacts are fabricated) to the cryogenic environment. Although the Ag drop has a diameter of at least $50\ \mu\text{m}$, the real electric contact occurs only between some of the Ag grains and the sample surface. The true contact is thus the parallel of several nanoscopic junctions that can well be in the ballistic regime (i.e. have a radius smaller than the electron mean free path). In Ref. [15] a rough evaluation of the mean free path in $\text{SmFe}_{1-x}\text{Ru}_x\text{AsO}_{0.85}\text{F}_{0.15}$ gave $\ell = 3 - 10$ nm without any clear dependence on the Ru content. In the cleaner samples with $x = 0.25$ and $x = 0.50$, the same evaluation gives $\ell \simeq 7$ nm and $\ell \simeq 20$ nm, respectively. Such small values of the mean free path make the fulfillment of the ballistic condition $a \ll \ell$ (where a is the contact radius) be very difficult to achieve. For instance, with these values of ℓ and the residual resistivities taken from table I, the Sharvin equation [22] would require resistances of the order of several $\text{k}\Omega$ for the contact to be ballistic. The typical experimental resistance of the contacts is instead in the range $10 - 100\ \Omega$. Indeed, many of the contacts were not spectroscopic or showed heating effects. A large number of measurements was then necessary to achieve a relatively small number of successful measurements. All the results reported here, except those shown in fig.3, are thus referred to the small fraction of contacts that do not show heating effects and gave a clear Andreev-reflection signal. In these cases, the existence of many parallel nanojunctions can be invoked to reconcile the actual contact resistance with the requirement of ballistic transport [21]. In some cases, the Sharvin condition was fulfilled at low temperature but broke down on increasing the temperature because of the decrease in the mean free path. In these cases, the values of the gaps at low temperature can be taken as meaningful anyway, though their temperature dependence and eventually the value of the local critical temperature can be slightly affected by the non-ideality of the contact.

RESULTS AND DISCUSSION

Point-contact Andreev-reflection results

Figure 2 reports the temperature dependence of the raw conductance curves (obtained by numerical differentiation of the $I - V$ characteristics) of one of the contacts that did not show any anomaly. The curves were measured in the $x = 0.10$ sample, and the normal-state resistance of the contact is around $50\ \Omega$. The curves show the

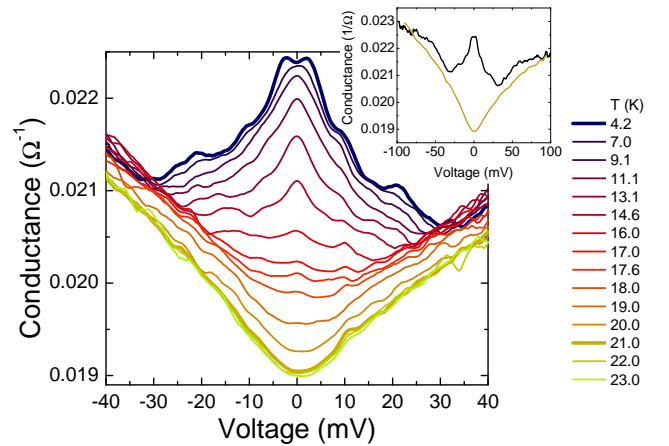


FIG. 2: Temperature dependence of the raw conductance curve of a point contact on the $x = 0.10$ sample. The normal state resistance is $R_N = 50\ \Omega$. The inset shows the curves at 4.2 K and at 21.0 K in an extended voltage range, to highlight the excess conductance persisting up to about 100 mV.

typical features already observed in $\text{SmFeAs}(\text{O}_{1-x}\text{F}_x)$ [23], in $\text{LaFeAs}(\text{O}_{1-x}\text{F}_x)$ [20] and in other 1111 compounds. In particular, they feature clear maxima related to a presumably nodeless gap, shoulders suggestive of a second larger gap and additional structures that, as recently shown [24], can be explained as being due to the strong electron-boson coupling. The excess conductance at high voltage, extending up to about 100 mV (see inset) is also typical of these systems [24]. The temperature at which the Andreev-reflection features disappear and the conductance becomes equal to the normal-state one is the local critical temperature of the contact, or Andreev critical temperature T_c^A . As shown in fig.2 this temperature is easy to identify in spectroscopic contacts because it also marks the point where conductance curves recorded at slightly different temperature start to be superimposed to one another (here the curves at 21.0, 22.0 and 23.0 K coincide within the experimental noise).

In contrast, Figure 3 reports two examples of conductance curves that show, together with an Andreev signal, deep and wide dips that, at low temperature, occur at energies comparable to those of the large gap. As shown elsewhere [21, 25] these dips are likely to be due to the current becoming overcritical in the region of the contact and prevent a proper determination of the gap amplitudes. On increasing temperature, they move toward lower voltage (due to the decrease of the critical current) causing an apparent shrinkage of the Andreev signal, finally giving rise to a sharp cusp at zero bias.

Going back to the case of ballistic contacts as in Fig.2, the conductance at or just above T_c^A can be used to normalize all the curves at $T < T_c^A$. In principle, a conductance curve recorded at a given temperature should be normalized to the normal-state conductance at the *same*

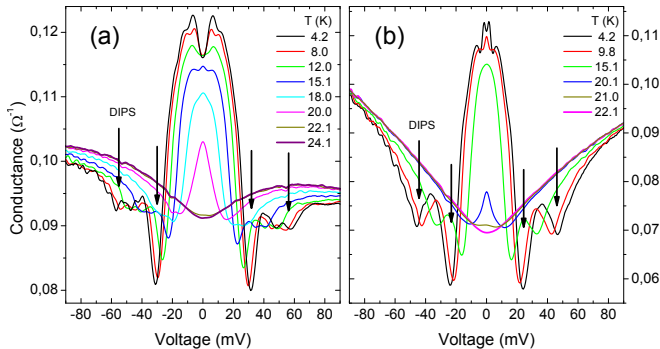


FIG. 3: Temperature dependence of two raw conductance curves in case of non ballistic contacts in the $x = 0.1$ sample. Dip features characteristic of non-ideal conduction through the contact are clearly visible; the conductance minima are indicated by arrows.

temperature, but because of the very high upper critical field of these materials, the latter is not usually accessible, at least at low T . Using the normal state at T_c^A to normalize all the curves is thus a somehow arbitrary choice but, as shown elsewhere [24], is anyway the one that preserves the weaker structures, i.e. those due to the large gap and, if present, those due to the strong electron-boson coupling.

Figure 4 shows some examples of low-temperature, normalized conductance curves in samples with different Ru content. Some important points are immediately clear by looking at these curves. First, none of them displays zero-bias peaks, and the same happens in 100% of the spectroscopic contacts. This points towards the absence of line nodes even at the highest Ru contents, contrary to what has been observed in some other FeBS away from optimal doping [7–10] [44]. Second, all the curves show more or less marked double-gap features. Third, despite the very large range of doping, the width of the structures does not change very much (note that all the panels have the same horizontal scale). Thus we should not expect major variations in the gap values upon Ru doping. Fourth, the asymmetry of the normalized conductance curves for positive/negative bias – which is particularly strong in unsubstituted $\text{SmFeAs}(\text{O}_{0.85}\text{F}_{0.15})$ [23] – seems to be reduced by Ru doping. As a matter of fact, it is clearly visible even at a first glance in the case $x = 0.05$, becomes discernible only while trying to fit the data in the cases $x = 0.10$ and $x = 0.25$ but almost completely disappears for $x = 0.30$ and $x = 0.50$. The real origin of this asymmetry, which is common to most point-contact spectra in Fe-based superconductors, is not completely clear yet, though it has been recently ascribed to the Seebeck effect [27]. Preliminary Seebeck

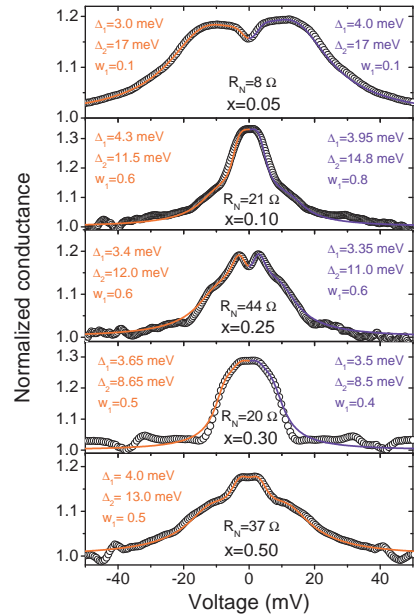


FIG. 4: Some examples of experimental conductance curves, after normalization (symbols), of point contacts on samples with different Ru content. The curves were all measured at 4.2 K. Solid blue (red) lines represent the best fit of the right (left) side of the experimental curves obtained within the two-band 2D generalized BTK model [24, 26]. The asymmetry decreases on increasing the Ru vanishing completely at $x = 0.50$. The fitting parameters are indicated in the labels.

effect measurements performed in these samples show indeed a considerable decrease of the Seebeck coefficient with increasing Ru content [28].

To extract quantitative information about the amplitude of the gaps from the conductance curves, they must be compared with suitable theoretical models. None of the models for single-band superconductivity can reproduce the shape of the experimental curves of fig.4. Instead, a two-band Blonder-Tinkham-Klapwijk model [29] generalized to the 2D case [26] and including a broadening term [30] is the minimal model that can be used in this case. For each band the parameters of the model are the energy gap Δ , the broadening parameter Γ and the barrier parameter Z . Then, being the total conductance the weighed sum of the single-band conductances, the last parameter is the weight w_1 of band 1 (the weight of band 2 being consequently determined as $1 - w_1$). [45] It is true that Sm-1111 is not two-dimensional and thus a 3D model should be used; however, as shown elsewhere [24], the latter is much more complicated and for any practical purpose one can safely use the 2D one (especially when, as it is the case here, the gaps are nodeless). The lines in Fig.4 represent the best fit of the experimental data, and the labels indicate the relevant values of the gaps and of the weight of band 1 in the point-contact

conductance, w_1 . To account for the residual asymmetry of the normalized curves, we chose to fit the positive- and negative-bias side separately (blue and red lines, respectively). As previously stated, for $x \geq 0.30$ the asymmetry is very small and the difference between the two fits can be no longer appreciated.

Figure 5 shows two examples of how the normalized conductance curves evolve with temperature, and the resulting temperature dependence of the gaps extracted from the fit. The two cases shown refer to a lightly doped sample ($x = 0.10$) and to a heavily doped one ($x = 0.50$). The lowest-temperature curves show clear shoulders related to the larger gap, which become less and less discernible in the other curves (vertically offset for clarity). In the $x = 0.50$ case, a dip structure is also seen to shift to lower energy on increasing the temperature, possibly giving rise to the small downward deviation of the temperature dependence of Δ_2 from a BCS-like $\Delta(T)$ curve observed at high temperature. Although there is no reason to expect the gaps to follow a BCS-like curve, the effects of the dip do not allow us to discuss whether this deviation is intrinsic or is an artifact due to the small mean free path of the samples. Incidentally, on the basis of recent calculations within a minimal three-band Eliashberg model [31] one would instead expect the gaps to be greater than the BCS value in proximity of the critical temperature.

Let us just recall here that the fitting procedure is generally not univocal, i.e. different sets of parameters can give almost equally good fits. Error bars in the insets to Fig.5 indicate the spread of gap values resulting from different fits.

Figure 6(a) shows the behavior of the gaps as a function of the Ru doping x . The data are rather scattered but a general trend is anyway discernible. While the small gap Δ_1 does not vary sensibly on increasing the Ru content x , the large gap Δ_2 shows a rapid decrease from $x = 0$ to $x = 0.10$ and then remains approximately constant. This behavior is in rough qualitative agreement with that of the bulk T_c reported in table I. Since PCARS is a local probe, the scattering of gap values at the same composition is most probably due to slight inhomogeneities in the local doping content. As long as T_c has a strong dependence on the doping content, i.e. up to $x = 0.25$, different point contacts on the same sample can thus provide different values of the gaps and of the local T_c^A , i.e. the Andreev critical temperature. As a matter of fact if one plots the gaps as a function of T_c^A as in fig.6(b), a roughly linear trend of both Δ_1 and Δ_2 can be appreciated despite the fluctuations in their values. It is worth reminding that the data reported here are already the results of a very careful selection aimed at eliminating all the questionable results, so that these fluctuations are not due to spurious effects that can be ascribed to non-ballistic conduction, heating, or spreading resistance. As for the large gap, a large uncertainty was

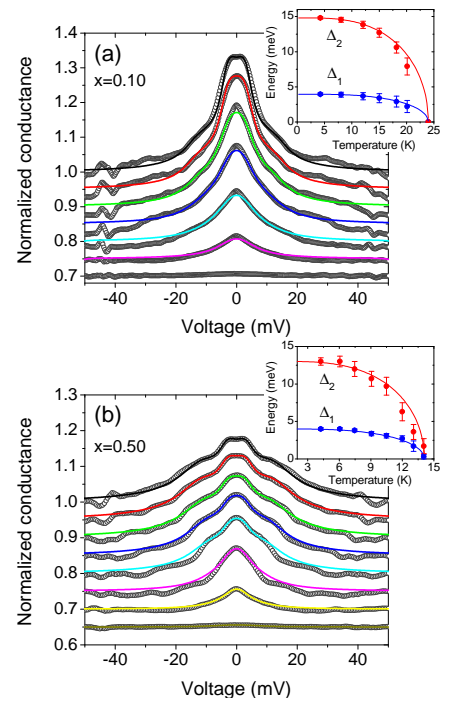


FIG. 5: Temperature dependence of the normalized conductance curves (symbols) of point contacts on the samples with $x = 0.10$ (a) and $x = 0.50$ (b) with the relevant two-band fit (lines). All the curves but the top ones are vertically shifted for clarity. The insets show the temperature dependence of the gaps Δ_1 and Δ_2 as extracted from the fit. The error bars indicate the spread of gap values obtained by different fits, when the other parameters (Γ_i , Z_i and the weight w_1 are changed as well).

also found in the starting compound $\text{SmFeAs}(\text{O}_{1-x}\text{F}_x)$ [23] (here represented by the vertical error bar on the point at the maximum T_c^A) and was ascribed to the residual degrees of freedom in the normalization process, to the asymmetry of the curves and to the fact that the features related to Δ_2 are less sharp than those related to the small gap Δ_1 . However, in the high-doping range ($x = 0.3$ and $x = 0.5$), T_c^A depends very little on the Ru content and the asymmetry has almost completely disappeared; even large differences in local composition correspond to a small difference in T_c^A . Therefore, the spread of gap values accompanied by a small spread in T_c^A seems to indicate a lack of correlation between these quantities (as observed also in MgB_2 with Al and Li co-doping [32]).

Since the gaps show an overall linear trend as a function of the local T_c^A , it is particularly instructive to plot the gap ratios $2\Delta_i/k_B T_c$ as a function of T_c^A . This is done in figure 7, which also reports various other PCARS data in 1111 and 122 compounds. Only results showing nodeless order parameters are shown for consistency. It is clear that the Ru substitution in the optimally F-doped Sm-1111 allows spanning a wide range of criti-

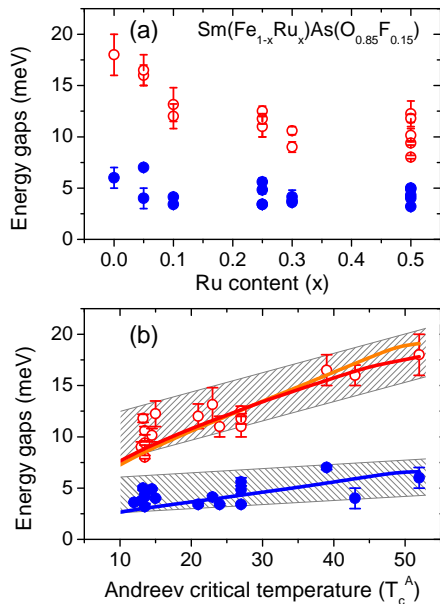


FIG. 6: (a) Energy gaps as extracted from the two-band fit of the conductance curves, as a function of the Ru content x . (b) Energy gaps as a function of the local critical temperature T_c^A of the various point contacts. Lines are gaps calculated within the three-band, $s\pm$ Eliashberg theory (see text for details).

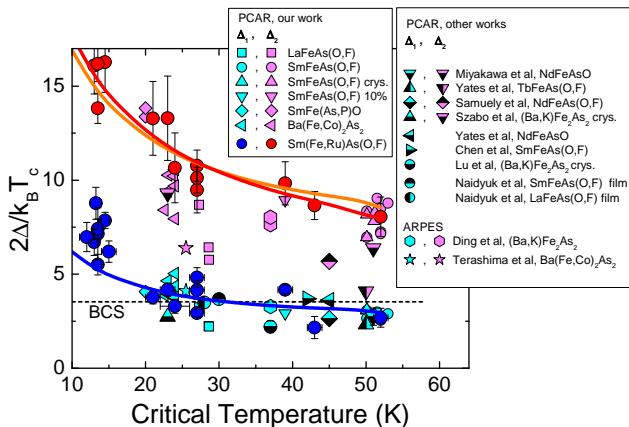


FIG. 7: Gap ratios $2\Delta_1/k_B T_c$ and $2\Delta_2/k_B T_c$ as a function of T_c as determined by point-contact Andreev-reflection spectroscopy in $\text{Sm}(\text{Fe}_{1-x}\text{Ru}_x)\text{AsO}_{0.85}\text{F}_{0.15}$ (blue and red circles) and in various other 1111 and 122 materials. Solid lines are $2\Delta_i/k_B T_c$ ratios calculated within the three-band, $s\pm$ Eliashberg theory (see text for details). Experimental data from literature are taken from ref. [24] and references therein.

cal temperatures, which not only covers but also extends the range of T_c values of superconducting Fe-based compounds measured so far by PCARS. As already shown in ref. [24], the $2\Delta_i/k_B T_c$ ratios start to increase below $T_c \sim 30$ K. Surprisingly, PCARS data *on this single sample series*, namely $\text{SmFe}_{1-x}\text{Ru}_x\text{AsO}_{0.85}\text{F}_{0.15}$, feature basically the same behavior as those obtained from many

other different nodeless FeBS of the 1111 and 122 families.

These results appear to be in contrast to what reported in ref. [33], where an opposite trend is suggested. However, even in the aforementioned paper, several results reported for FeBS show $2\Delta/k_B T_c$ ratios which seem to increase with decreasing T_c , particularly for the large gap. A definitive answer on the possibility of a universal trend of $2\Delta_i/k_B T_c$ vs. T_c requires more experimental work, comparing results obtained with different techniques on samples of increasingly better quality.

Electronic structure calculations

In order to try to explain the observed PCARS data within the Eliashberg theory, we preliminarily performed electronic structure calculations. In particular, SmFeAsO electrons and holes density of states (DOS) have been obtained by *ab initio* calculations performed in the local density approximation to the density-functional theory (LDA-DFT) [34] as implemented in the all-electron full-potential APW and local orbitals [35, 36] code Wien2k [37]. APW has the advantage to treat explicitly $\text{Sm } 4f$ electrons within the valence band yielding state-of-the-art band structure dispersion quality. To simulate Ru substitution our calculations were performed in a tetragonal super-cell containing four formula units ($Pma2$ No. 28) where 25% Ru concentration was achieved by the substitution of one Ru out of four Fe, retaining the bulk symmetry in the defected cell. The conservation of symmetry allowed a reliable comparison of doped and undoped band structures without folding/unfolding mapping problems. Muffin tin radii of 2.3, 1.9, 2.2 and 2.0 Bohr were used for Sm, O, Fe and As, respectively. Brillouin zone integration was performed with tetrahedrons on a $6 \times 6 \times 4$ mesh [38]. Since we are interested in the superconducting paramagnetic phase of SmFeAsO , Fe spin polarization was not considered. The relevant band structure of this system is given by two electron and three hole bands as it is usual for 1111 ironpnictides. Those are superimposed to the $4f$ Sm bands at the Fermi energy (E_F). To disentangle the contribution of the Fe $3d$ bands we used the so-called *fat-band* representation by projecting the wavefunction onto the Fe atomic orbitals and thus obtaining the band structures shown by dots in Fig.8. The size of dots is proportional to the d atomic character of the wavefunction on Fe atoms.

Such a procedure allows to identify a number of parabolic Fe $3d$ bands around E_F . Since comparison with LaFeAsO is relevant, in Fig.8(a) we report the band structure obtained for the same crystal structure of the SmFeAsO compound where Sm has been replaced by La. In Fig.8(a) we clearly see the usual set of five parabolic Fe d bands, two electrons (e_1, e_2) and three holes ones (h_1, h_2 and h_3), all of them centered at the Γ point since

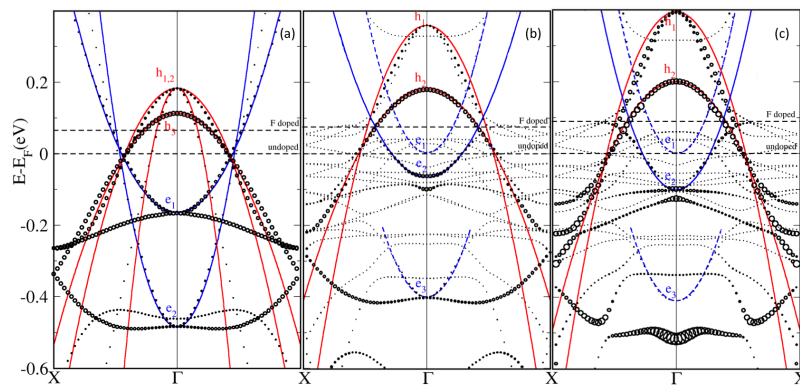


FIG. 8: Color online. $\text{SmRu}_x\text{Fe}_{1-x}\text{AsO}$ fat-band structure in the four formula unit super-cell. Dots are proportional to the Fe $3d$ character of the wavefunctions. Parabolas show the results of a fit of the Fe $3d$ bands within the two-dimensional electron gas model. Upper and lower horizontal dashed lines are E_F with and without F doping, respectively. a) Reference band structure with La replacing Sm. b) Actual SmOFeAs band structure including the $4f$ Sm bands. The two light holes bands have similar dispersions and have been fitted with a single parabola h_1 . c) Same as in b) but in the case of $\text{SmFe}_{0.75}\text{Ru}_{0.25}\text{AsO}$. In b) and c) the parabolic fit of band e_3 is shown only up to an energy close to the one where its hybridization with Sm $4f$ bands takes place.

we are using a four formula unit super-cell. This finding is in agreement with previous LDA-DFT calculations provided we consider that SmFeAsO structure was used here [3]. As for the band structure of the actual SmFeAsO , we find Fe d bands superimposed to Sm $4f$ ones. This fact not only makes the interpretation of the band structure less easy but introduces a hybridization effect between Sm and Fe states. LDA bands in Fig.8(b) show that Fe electron bands in SmFeAsO are no more simply parabolic but hybridization introduces warping out of the central part of the Brillouin zone. Hybridization splits the electron band labeled e_2 in Fig.8(a) in two pieces named e_3 and e_1 in Fig.8(b). In undoped SmFeAsO e_3 and e_1 do not cross E_F being the former too low in energy and hybridized with Sm $4f$ bands (see details of Fig.8(b)) and the upper too high. Therefore, undoped SmFeAsO will have only one Fe-derived electron band e_2 and three hole ones, the doubly-degenerate light-hole h_1 and the heavy-hole h_2 . The Fermi surface will be made of four nearly cylindrical sheets, one less than LaFeAsO . Such a finding seems to be in agreement with ARPES measurements on SmFeAsO where only one electron band is suggested [39]. Since in the Eliashberg approach we are interested in the Fe d states DOS, we need to disentangle that contribution out of the total one that includes the Sm $4f$ bands. Our choice is to model the band structure as a superposition of five parabolic bands (including the empty e_1) inside the background of $4f$ states. With the help of the fat-band representation, we fitted the relevant bands along the Γ -X direction (Γ -M in the usual two-formula unit cell) with parabolas shown as solid and dashed lines in Fig.8. Disregarding the possible warping of the cylindrical Fermi surfaces, the DOS deriving from the above mentioned bands was estimated from the

calculated effective masses by the free two-dimensional electron gas model $N(E) = m^*/\pi\hbar^2$. This approximation is even more justified by the fact that in the Eliashberg analysis reported below only ratios between DOSs (which are much more accurate) enter in the calculations. Then, given this assumption, only the band curvature is relevant and therefore energy shifts with respect to LDA are not important in the model. The only important difference relies on the fact that the number of parabolic bands taken into consideration is five or four. In this regard, the position of E_F is critical since band e_1 is just above E_F in the undoped compound. The superconducting phase is obtained by 15% F doping i.e. in $\text{SmFeAsO}_{0.85}\text{F}_{0.15}$. F substitution adds electrons to the system and in the rigid band approach such effect can be coped by the rigid shift of E_F by 0.15 electrons per formula unit. Given the DOS $N(E)$ of the system, the shift can be simply estimated as $0.15/N(E_F)$. Anyway, care should be taken in defining $N(E)$, since the localized nature of Sm $4f$ orbitals makes it likely that they do not receive the additional doping charge from F. We therefore filtered out this contribution from $N(E)$ considering only the contribution of bands $e_{1,2}$ and $h_{1,2}$. Following this approach we get a sort of upper bound for the E_F shift to be about 75 meV (90 meV) for $\text{SmFeAsO}_{0.85}\text{F}_{0.15}$ ($\text{SmFe}_{0.75}\text{Ru}_{0.25}\text{AsO}_{0.85}\text{F}_{0.15}$). The Fermi levels E_F of F-doped and undoped SmFeAsO and $\text{SmFe}_{0.75}\text{Ru}_{0.25}\text{AsO}$ are shown in Fig.8(a)-(c). We see that in the F-doped systems the band e_1 is always partially filled justifying our assumption to include its contribution in Eliashberg calculations. As for the effect of Ru substitution, by comparing Fig.8(b) and (c) we see that the effect is modest, only band e_2 is a bit deeper and with lower effective mass as shown in Fig.8(c). Calculated DOS and plasma fre-

$x = 0$	m_{eff}	DOS (st/Ha/Bohr ²)	ω_p (meV)
e_1	0.739	0.2352	714.04
e_2	1.508	0.4800	975.56
h_1	0.908	0.2890	1391.91
h_2	2.057	0.6547	844.86
<hr/>			
$x = 0.25$			
e_1	0.668	0.2127	782.19
e_2	0.882	0.2809	1136.49
h_1	0.957	0.3048	1428.07
h_2	1.736	0.5526	864.74

TABLE II: Calculated effective masses, DOS and plasma frequencies for $\text{SmFe}_{1-x}\text{Ru}_x\text{AsO}_{0.85}\text{F}_{0.15}$ at doping levels $x = 0$ and $x = 0.25$. h_1 is doubly degenerate.

quencies for each band and for the two doping levels considered are reported in table II.

Analysis of experimental results within Eliashberg theory

Based on the results of band structure calculations described so far, it is possible to propose an explanation of the experimental data by means of the simplest model that allows describing the essential physics of the materials under study. We used the three-band, \pm Eliashberg theory [31] taking into account the feedback effect [40]. Within this model we have two hole bands (from now on labeled as 1 and 2) and one equivalent electron band (labeled as 3). The free parameters are $N_i(0)$, λ_{31} , λ_{32} , $\Omega(T)$ and Γ . $N_i(0)$ is the DOS at Fermi level, calculated above for $x = 0$ and $x = 0.25$ and obtained at all the other doping levels by linear interpolation as a function of the experimental T_c ; λ_{31} and λ_{32} are the electron-boson coupling constants between band 3 and band 1 or 2, respectively; $\Omega(T)$ is the representative boson energy that we take as $\Omega(T) = \Omega_0 \tanh(1.76k\sqrt{(T_c^*/T) - 1})$ where $\Omega_0 = 2T_c/5$ [41]; the electron-boson spectral function has a Lorentzian shape [31] with halfwidth $\Gamma = \Omega_0/2$ [6]; T_c^* is the feedback critical temperature, determined by solving the Eliashberg equations in the imaginary-axis formulation. The electron-boson coupling matrix is

$$\begin{pmatrix} 0 & 0 & \lambda_{31}\nu_1 \\ 0 & 0 & \lambda_{32}\nu_1 \\ \lambda_{31} & \lambda_{32} & 0 \end{pmatrix}$$

where $\nu_1 = N_3(0)/N_1(0)$ and $\nu_2 = N_3(0)/N_2(0)$. k was determined at $x = 0$ in the following way: first, the superfluid density was calculated by using the plasma frequencies obtained from first principles and reported in table II, giving also the correct T_c . Then, since the temperature-dependent part of the superfluid density corresponds to that of the representative boson frequency

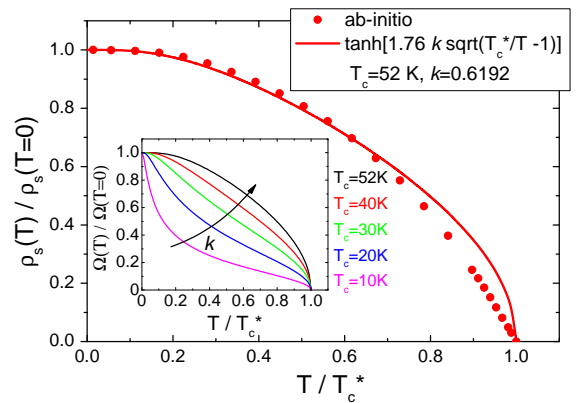


FIG. 9: Temperature-dependent part of the superfluid density, $\rho_s(T)/\rho_s(T = 0)$ (symbols) calculated by using the plasma frequencies obtained from first principles calculations (see table II) in $\text{SmFe}_{1-x}\text{Ru}_x\text{AsO}_{0.85}\text{F}_{0.15}$ for $x=0$ ($T_c=52$ K). The line is a fit with the formula $\tanh(1.76k\sqrt{(T_c^*/T) - 1})$, giving $k = 0.6192$. Inset: temperature-dependent part of the superfluid density (and therefore of the representative boson frequency [40]) used in the Eliashberg calculations at different critical temperatures (see text for details).

[40], this curve was fitted with $\tanh(1.76k\sqrt{(T_c^*/T) - 1})$, giving $k = 0.6192$. The values of the calculated superfluid density and the relevant fit are shown in Fig. 9 as symbols and line, respectively.

At this point, the only parameters that remain to be determined are two: λ_{31} , λ_{32} . At $x = 0$ they are obtained by reproducing the two experimental gaps, but it turns out that they also reproduce the exact experimental critical temperature. Then we assume that the ratio $\lambda_{31}/\lambda_{32}$ is doping-independent and that k is a linear function of the experimental critical temperature: $k(T_c) = k(T_{c,x=0})T_c/T_{c,x=0}$. This assumption is related to the temperature dependence of the superfluid density and is reasonable to suppose that with increasing x (and therefore decreasing of T_c) it decreases [8]. Now, the only free parameter left in the process of fitting the T_c dependence of the gaps is λ_{31} which is fixed by obtaining T_c coincident with the experimental one. The procedure is self-consistent since λ_{31} is varied until T_c^* , introduced in the formula for $\Omega(T)$, allows reproducing the experimental T_c . Disorder effects have been neglected as impurities are dominant in the intraband channel and are thus not pair-breaking. Moreover, we also assumed that, as a first approximation, they are also absent in the interband channel since the two gaps are well distinct at all doping levels.

Results are shown in Fig. 6(b) as solid lines: the calculated gap values follow rather well the trend of the experimental ones at all temperatures. The same good agreement with the experiment can be seen also by looking at the $2\Delta_i/k_B T_c$ ratios as a function of T_c shown in Fig. 7 which also reports many other results from the

literature. In this regard, it is also remarkable that it is possible, with a relatively simple model and a small number of free parameters, to reproduce the increase of the ratio with decreasing T_c . Since the strength of the coupling increases with decreasing T_c , the same does, as expected, the total electron-boson coupling constant, λ_{tot} which is about 3.2 at $T_c=52$ K and goes up to almost 7.3 when $T_c=10$ K. Another interesting result that comes out from the theoretical analysis is the temperature dependence of the representative boson frequency (shown in the inset to Fig. 9 for different critical temperatures) which, as already stated above, is equivalent to that of the superfluid density [40]. We can notice that, as T_c decreases, the superfluid density also decreases as a function of T assuming, below $T_c=30$ K, a positive curvature at intermediate temperatures. Similar dependencies (at least in the low- and mid- T_c range) have been obtained in penetration depth measurements in Co-doped Ba-122 samples, as reported in ref. [8]. In that case the effect is less pronounced probably because the results are reported only down to about $2T_c/5$ while in our case T_c drops to $T_c/5$ at the highest Ru doping. Moreover, it is also interesting to notice that in Co-doped Ba-122 the temperature dependence of the superfluid density looks slightly more depressed in samples that belong to the region of coexistence of superconductivity and magnetism. This fact leads us to speculate that the observed behavior of the superfluid density in our samples might be considerably influenced by the onset of a short-range magnetic order which competes with superconductivity and that has been observed by μ SR and ^{75}As NQR measurements in the same samples [19]. Penetration depth measurements, as the ones in ref. [8], would help clarifying this point as well as the experimental determination of the temperature dependence of the representative boson frequency, as done in refs. [6, 24, 42].

CONCLUSIONS

The isoelectronic substitution of Fe with Ru in optimally F-doped Sm-1111 is a good way to explore a very wide range of critical temperatures within the same Fe-based compound, in principle without changing the total charge of the system [15]. The considerable decrease of T_c induced by Ru substitution has been ascribed to disorder in the Fe sub-lattice [15] and/or to the onset of a short-range magnetic order [19]. Here we have shown that, in a wide range of T_c (from 52 K down to 13.5 K, corresponding to Ru contents ranging from 0 to 50 %) the $\text{Sm}(\text{Fe}_{1-x}\text{Ru}_x)\text{AsO}_{0.85}\text{F}_{0.15}$ system retains its original multi-gap character, and also the symmetry of the gaps remains nodeless. The amplitudes of the two experimentally detectable gaps, Δ_1 and Δ_2 , decrease almost linearly with T_c , but they remain well distinct down to the lowest T_c . This suggests that the substitution-

induced disorder mainly enhances intraband scattering and does not significantly affect the interband one. The gap ratios $2\Delta_i/k_B T_c$ strongly increase for $T_c < 30$ K in a manner which suggests an unexpected increase of the electron-boson coupling when T_c is depressed. Very interestingly, the trend of the gap ratios as a function of T_c in this single system is superimposed to the analogous trend obtained by plotting the data of many Fe-based compounds of different families [24]. Needless to say, this seems to point towards a general, universal property of this class of superconductors. By using the values of the density of states and of the plasma frequencies calculated from first principles, we have shown that the *increase* in the gap ratios $2\Delta_i/k_B T_c$ on decreasing T_c can be reconciled with a spin-fluctuation-mediated pairing even though the characteristic spin-fluctuation energy has been observed to *decrease* linearly with T_c . The key to solving this puzzle is the feedback effect, i.e. the effect of the condensate on the mediating boson, which is of course only expected when the superconducting pairing between electrons is mediated by electronic excitations [40]. An analysis carried out within an effective three-band Eliashberg model shows indeed that the experimental dependence of the gaps (and of the gap ratios $2\Delta_i/k_B T_c$) on T_c can be explained as being due, in particular, to a change in the shape of the temperature dependence of the characteristic boson energy, $\Omega_0(T)$, with respect to the optimal- T_c compound (with no Ru). Indeed, a suppression of Ω_0 in the mid-temperature range (which becomes more and more sensible on decreasing T_c) is required to obtain the correct critical temperature and the correct gap values. This finding is in very good qualitative agreement with the experimental observation of a depression of the superfluid density in Co-doped Ba-122 with reduced T_c [8]. The fact that in the latter case this reduction is observed in underdoped samples that fall in the region of coexistence of magnetism and superconductivity further suggests that, also in our samples, the depression of the condensate (that in turns gives rise to a depression in the boson energy) at finite temperature may be considerably influenced by the onset of a short-range magnetic order competing with superconductivity induced by Ru substitution, as recently observed by μ SR and ^{75}As NQR measurements in the same set of samples [19].

ACKNOWLEDGEMENTS

This work was done within the PRIN project No. 2008XWLWF9-005. FB acknowledges support from CASPUR under the Standard HPC Grant 2012.

-
- [1] Y. Kamihara, T. Watanabe, M. Hirano, and H. Hosono, *J. Am. Chem. Soc.* **130**, 3296 (2008).
- [2] I. I. Mazin and J. Schmalian, *Physica C* **469**, 614 (2009).
- [3] I. I. Mazin, M. D. Johannes, L. Boeri, K. Koepernik, and D. J. Singh, *Phys. Rev. B* **78**, 085104 (2008).
- [4] I. I. Mazin, D. J. Singh, M. D. Johannes, and M. H. Du, *Phys. Rev. Lett.* **101**, 057003 (2008).
- [5] C.-T. Chen, C. C. Tsuei, M. B. Ketchen, Z.-A. Ren, and Z. X. Zhao, *Nature Phys.* **6**, 260 (2010).
- [6] D. S. Inosov, J. T. Park, P. Bourges, D. L. Sun, Y. Sidis, A. Schneidewind, K. Hradil, D. Haug, C. T. Lin, B. Keimer, et al., *Nature Phys.* **6**, 178 (2010).
- [7] J.-P. Reid, M. A. Tanatar, X. G. Luo, H. Shakeripour, N. Doiron-Leyraud, N. Ni, S. L. Budko, P. C. Canfield, R. Prozorov, and L. Taillefer, *Phys. Rev. B* **82**, 064501 (2010).
- [8] R. Prozorov and V. G. Kogan, *Rep. Prog. Phys.* **74**, 124505 (2011).
- [9] J.-P. Reid, M. A. Tanatar, X. G. Luo, H. Shakeripour, S. René de Cotret, N. Doiron-Leyraud, J. Chang, B. Shen, H.-H. Wen, H. Kim, et al. (2011), unpublished, arXiv:1105.2232.
- [10] P. J. Hirschfeld, M. M. Korshunov, and I. I. Mazin, *Rep. Prog. Phys.* **74**, 124508 (2011).
- [11] K. Kuroki, H. Usui, S. Onari, R. Arita, and H. Aoki, *Phys. Rev. B* **79**, 224511 (2009).
- [12] S. C. Lee, A. Kawabata, T. Moyoshi, Y. Kobayashi, and M. Sato, *J. Phys. Soc. Jpn.* **78**, 043703 (2009).
- [13] A. S. Sefat, A. Huq, M. A. McGuire, R. Jin, B. C. Sales, D. Mandrus, L. M. D. Cranswick, P. W. Stephens, and K. H. Stone, *Phys. Rev. B* **78**, 104505 (2008).
- [14] H.-H. Wen, G. Mu, L. Fang, H. Yang, and X. Zhu, *Europhys. Lett.* **82**, 17009 (2008).
- [15] M. Tropeano, M. R. Cimberle, C. Ferdeghini, G. Lamura, A. Martinelli, A. Palenzona, I. Pallecchi, A. Sala, I. Sheikin, F. Bernardini, et al., *Phys. Rev. B* **81**, 184504 (2010).
- [16] N. D. Zhigadlo, S. Katrych, M. Bendele, P. J. W. Moll, M. Tortello, S. Weyeneth, V. Y. Pomjakushin, J. Kanter, R. Puzniak, Z. Bukowski, et al., *Phys. Rev. B* **84**, 134526 (2011).
- [17] M. A. McGuire, D. J. Singh, A. S. Sefat, B. C. Sales, and D. Mandrus, *J. Solid State Chem.* **182**, 2326 (2009).
- [18] S. C. Lee, E. Satomi, Y. Kobayashi, and M. Sato, *J. Phys. Soc. Jpn.* **79**, 023702 (2010).
- [19] S. Sanna, P. Carretta, P. Bonfà, G. Prando, G. Allodi, R. De Renzi, T. Shiroka, G. Lamura, A. Martinelli, and M. Putti, *Phys. Rev. Lett.* **107**, 227003 (2011).
- [20] R. S. Gonnelli, D. Daghero, M. Tortello, G. A. Um-
marino, V. A. Stepanov, J. S. Kim, and R. K. Kremer, *Phys. Rev. B* **79**, 184526 (2009).
- [21] D. Daghero and R. Gonnelli, *Supercond. Sci. Technol.* **23**, 043001 (2010).
- [22] Y. V. Sharvin, *Zh. Eksp. Teor. Fiz.* **48**, 984 (1965), engl. *Transl. Sov. Phys.-JETP* **21**, 655 (1965).
- [23] D. Daghero, M. Tortello, R. S. Gonnelli, V. A. Stepanov, N. D. Zhigadlo, and J. Karpinski, *Phys. Rev. B* **80**, 060502(R) (2009).
- [24] D. Daghero, M. Tortello, G. Um-
marino, and R. S. Gonnelli, *Rep. Prog. Phys.* **74**, 124509 (2011).
- [25] G. Sheet, S. Mukhopadhyay, and P. Raychaudhuri, *Phys. Rev. B* **69**, 134507 (2004).
- [26] S. Kashiwaya, Y. Tanaka, M. Koyanagi, and K. Kajimura, *Phys. Rev. B* **53**, 2667 (1996).
- [27] Y. G. Naidyuk, O. E. Kvitnitskaya, I. K. Yanson, G. Fuchs, S. Haindl, M. Kidszun, L. Schultz, and B. Holzapfel, *Supercond. Sci. Technol.* **24**, 065010 (2010).
- [28] M. Putti et al., in preparation.
- [29] G. E. Blonder, M. Tinkham, and T. M. Klapwijk, *Phys. Rev. B* **25**, 4515 (1982).
- [30] A. Plecenik, M. Grajcar, v. Beňačka, P. Seidel, and A. Pfuch, *Phys. Rev. B* **49**, 10016 (1994).
- [31] G. A. Um-
marino, M. Tortello, D. Daghero, and R. S. Gonnelli, *Phys. Rev. B* **80**, 172503 (2009).
- [32] G. A. Daghero, D. Um-
marino, M. Tortello, D. Delaude, R. S. Gonnelli, V. A. Stepanov, M. Monni, and A. Palenzona, *Supercond. Sci. Technol.* **22**, 025012 (2009).
- [33] D. S. Inosov, J. T. Park, A. Charnukha, Y. Li, A. V. Boris, B. Keimer, and V. Hinkov, *Phys. Rev. B* **83**, 214520 (2011).
- [34] J. P. Perdew and Y. Wang, *Phys. Rev. B* **45**, 13244 (1992).
- [35] D. Singh, *Phys. Rev. B* **43**, 6388 (1991).
- [36] E. Sjöstedt, L. Nordström, and D. J. Singh, *Solid State Commun.* **114**, 15 (2000).
- [37] B. Blaha, K. Schwarz, G. K. H. Madsen, D. Kvasnicka, and J. Luitz, *WIEN2k: An Augmented Plane Wave Plus Local Orbitals Program for Calculating Crystal Properties*, Techn. Universitt Wien, Wien, Austria (2001), see <http://www.wien2k.at>.
- [38] P. E. Blöchl, O. Jepsen, and O. K. Andersen, *Phys. Rev. B* **49**, 16223 (1994).
- [39] L. Yang, B. Xie, B. Zhou, Y. Zhang, Q. Ge, F. Wu, X. Wang, X. Chen, and D. Feng, *J. Phys. Chem. Solids* **72**, 460 (2011).
- [40] G. A. Um-
marino, *Phys. Rev. B* **83**, 092508 (2011).
- [41] J. Paglione and R. L. Greene, *Nature Phys.* **6**, 645 (2010).
- [42] M. Tortello, D. Daghero, G. A. Um-
marino, V. A. Stepanov, J. Jiang, J. D. Weiss, E. E. Hellstrom, and R. S. Gonnelli, *Phys. Rev. Lett.* **105**, 237002 (2010).
- [43] A. A. Golubov, A. Brinkman, Y. Tanaka, I. I. Mazin, and O. V. Dolgov, *Phys. Rev. Lett.* **103**, 077003 (2009).
- [44] Moreover, none of the curves we measured showed the finite-energy peaks associated with quasiparticle interference predicted, in some conditions, in the nodeless $s\pm$ symmetry [43]. The occurrence and the voltage position of these peaks is controlled, in the relevant theory, by a mixing parameter α which has not been related yet to experimental parameters. Therefore, either these peaks are not present because the conditions for their observation are not fulfilled, or they are smeared out, particularly at the Z values typical of our contacts, by the broadening effects.
- [45] The BTK model provides reliable results also in the case of parallel nano-junctions. Simulations show that the fit of the total conductance in this case gives “effective” parameters. The “effective” gap turns out to be approximately equal to the average of the gaps of the individual contacts.